minerals

MDPI

Article

X-ray Laue Microdiffraction and Raman Spectroscopic Investigation of Natural Silicon and Moissanite

Camelia Veronica Stan [1,*], Earl Francis O'Bannon III [2,*], Pavel Mukhin [3], Nobumichi Tamura [4] and Larissa Dobrzhinetskaya [5]

1 NIF & Photon Science Directorate, Lawrence Livermore National Laboratory, PO Box 808, Livermore, CA 94551, USA
2 Physical and Life Sciences Directorate, Lawrence Livermore National Laboratory, PO Box 808, Livermore, CA 94551, USA
3 Independent Consultant in Ore Deposits, Tel Aviv 2067041, Israel; pavelmukhin4@gmail.com
4 Advanced Light Source, Lawrence Berkeley National Laboratory, 1 Cyclotron Road, Berkeley, CA 94720, USA; ntamura@lbl.gov
5 Earth and Planetary Sciences, University of California Riverside, 900 University Avenue, Riverside, CA 92521, USA; larissa@ucr.edu
* Correspondence: stan2@llnl.gov (C.V.S.); obannon2@llnl.gov (E.F.O.III)

Received: 30 January 2020; Accepted: 21 February 2020; Published: 25 February 2020

Abstract: Moissanite, SiC, is an uncommon accessory mineral that forms under low oxygen fugacity. Here, we analyze natural SiC from a Miocene tuff-sandstone using synchrotron Laue microdiffraction and Raman spectroscopy, in order to better understand the SiC phases and formation physics. The studied crystals of SiC consist of 4H- and 6H-SiC domains, formed from either, continuous growth or, in one case, intergrown, together with native Si. The native Si is polycrystalline, with a large crystal size relative to the analytical beam dimensions (>1–2 μm). We find that the intergrown region shows low distortion or dislocation density in SiC, but these features are comparatively high in Si. The distortion/deformation observed in Si may have been caused by a mismatch in the coefficients of thermal expansion of the two materials. Raman spectroscopic measurements are discussed in combination with our Laue microdiffraction results. Our results suggest that these SiC grains likely grew from an igneous melt.

Keywords: SiC; Laue diffraction; microdiffraction; natural silicon; moissanite; Si; synchrotron; polymorph; mineral deformation

1. Introduction

SiC may be the archetypal polytypic material (e.g., polymorphs only differ in the stacking sequence of identical sheets or structural units) with greater than 250 known synthetic polytypes, ~11 of which are reported as naturally occurring [1]. The polytypes are typically described with a number that refers to the number of layers that repeat along the stacking direction, and a letter that refers to the crystal system [2]. They generally lie on a continuum between the wurtzite (2H) and zinc-blende (3C) structures, depending on the relative interplanar layering of Si and C. Figure 1 shows the stacking sequence of three of the simplest naturally-occurring polytypes of SiC. Moissanite, the naturally occurring SiC mineral, is typically considered to be either, the 6H- or, to a lesser extent, 4H- and 15R-SiC structure types. Predicting which polytype forms under natural conditions is complicated, and currently there are several well-summarized theories to explain formation [3], ranging from thermodynamic, kinetic, and growth considerations. Moreover, transformation from one polytype to another is thought to occur by periodic slip around dislocations [4], diffusional rearrangement with the nucleation and expansion of stacking faults [5], and/or changes in Si/C ratios during crystallization [6].

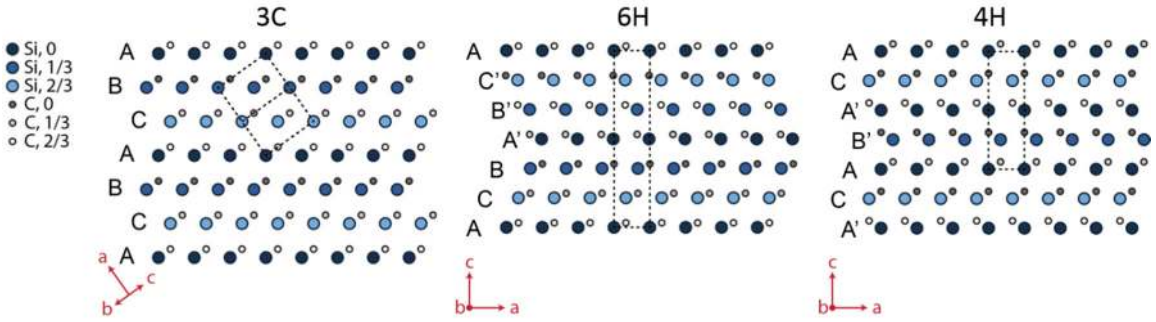

Figure 1. 3C-, 6H- and 4H-SiC structures can be interpreted through the orientation of alternating Si and C layers [7,8]. The unit cell in each case is represented by a dashed line. The layers are labelled based on relative stacking position and depth coming out of the page.

Naturally occurring moissanite (SiC) was first discovered within the impact rocks of the Canyon Diablo meteor crater of Arizona [9]. Moissanite was once considered a geological aberration [10]. Many synthetic routes have been reported (see review by Abderrazak and Hmida [11]), with variations in the resulting crystal properties, but none truly mimic geological conditions, which range from relatively low pressure (upper crust) to high pressure (mid to lower mantle), high temperature, and very low oxygen fugacity. For more than a century, natural occurrences of moissanite have been reported in the literature and these reports show that SiC origin may be broken up into three categories: (i) high-, ultra-high pressure environments, such as upper- and lower mantle and mantle transition zone, and even core–mantle boundary; (ii) ambient/low-pressure environments, such as metamorphic, magmatic rocks and hydrothermal processes recorded in both continental and oceanic crust; or (iii) formation of SiC and native metals during lightning strikes in the ophiolitic rocks exposed on the Earth's surface [12–20]. All require temperature ranged from 700–800 °C to 2500 °C, and extremely low oxygen fugacity, e.g. ~8 to <12 log-bar units [21], or 6 to 8 log-bar units [22] below the iron-wüstite (IW) buffer. In the last two decades many more well-documented, including in-situ, finds of natural moissanite have been reported [12–18,23–43]. These reports suggest that moissanite may be a much more common accessory mineral than previously thought. More analytical data and measurements from well-documented *in situ* natural SiC are necessary in formulating a less incontrovertible mechanism of moissanite formation under geological conditions.

Here, we analyze naturally-occurring SiC in a tuff-sandstone, focusing on the understanding of the mechanism of SiC formation, and on the intrinsic relationship between SiC and Si, recorded in one of the studied moissanite grains. We employ X-ray Laue microdiffraction (μXRD) and Raman spectroscopy to investigate the microstructure, distortion, and phase relations in both SiC and Si.

2. Materials and Methods

2.1. Sample Description

The sample is a lithified tuff-sandstone (also referred to as tuffite) related to the Miocene age Lower Basalt Formation in the Yizre'el Valley of Kishon River, Israel. The rock includes fragments of local sediments mixed with the pyroclastic material deposited during volcanic eruption (e.g., Baer et al., [44]). The research sample consists of the hypidiomorphic crystals of picroilmenite, magnetite and ulvospinel intermixed with eroded round crystals of quartz and anorthite, all of which are cemented with secondary Ca, Fe, Mg-hydrous carbonates, chlorite and serpentine (see detailed description in Dobrzhinetskaya et al., [41]). The thin section used for this research is a piece of the same sample, described in Dobrzhinetskaya et al., [41] as tuffite. However, it can be now identified more precisely as a tuff-sandstone, due to presence of a microfossil (Figure 2a). The rock was cut by a diamond mini-saw and mounted into an epoxy disc followed by polishing with 50 μm, 15 μm, and 3 μm size corundum pastes and ultrasonic rinsing in distilled water after each step of polishing. The SiC crystals were

identified with the aid of optical microscopy and Raman spectroscopy. Three grains of moissanite, labelled SiC1, SiC2—containing native Si inclusions, and SiC3, were chosen for analysis (Figure 2a–d).

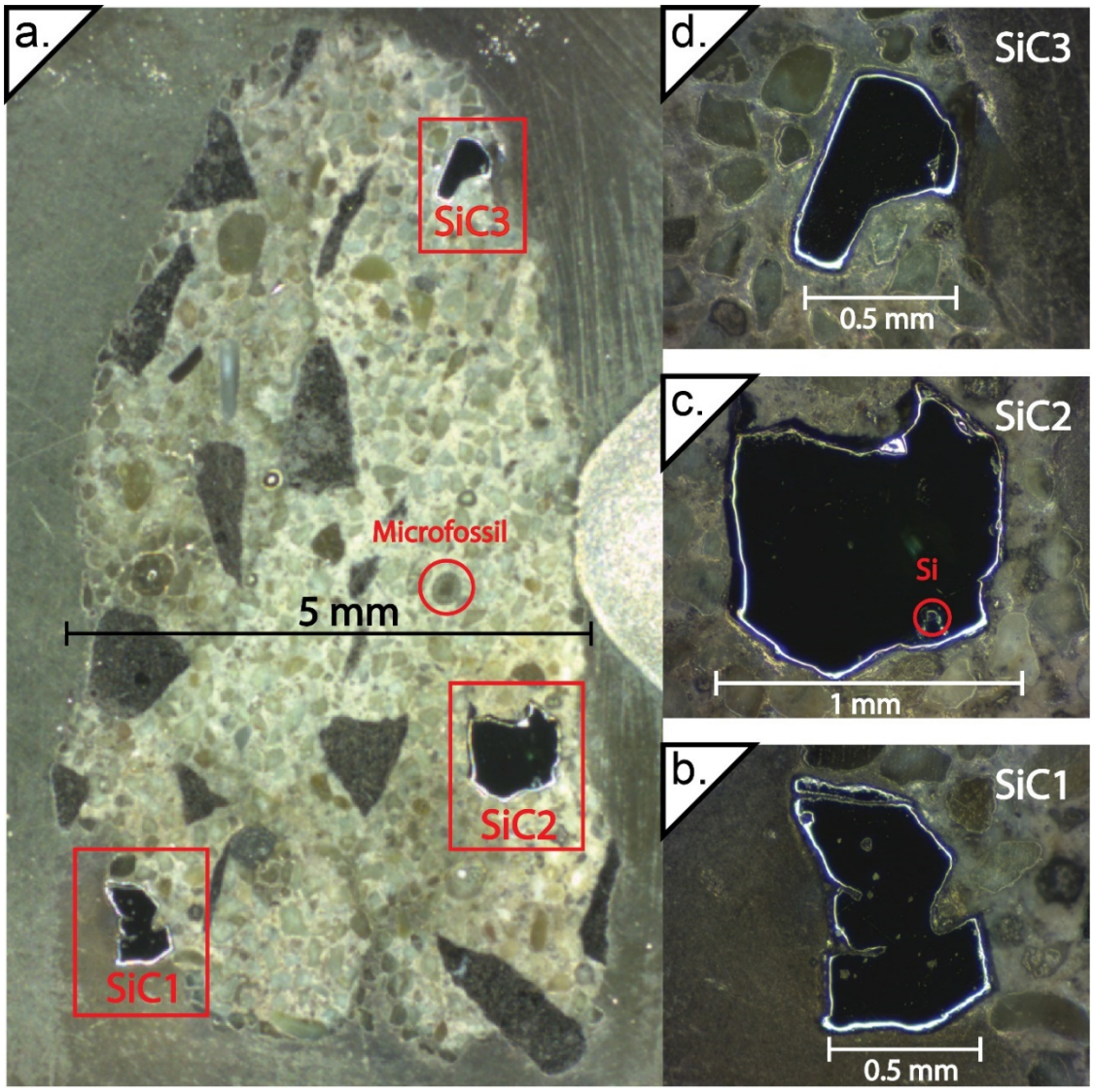

Figure 2. (**a**) The microscope image of the sample clearly shows the location of the SiC grains (**b**–**d**), which have different reflectivities from the surrounding rock matrix. The red circle indicates the location of a microfossil (Figure S1). Locations of SiC grains in a. and the Si inclusion in SiC2 (**c**)are indicated.

2.2. Data Collection

X-ray fluorescence (XRF) and μXRD were collected at beamline 12.3.2 of the Advanced Light Source at Lawrence Berkeley National Laboratory. A white light beam (5–24 keV) was focused to an area of ~1 μm × 1 μm using Kirkpatrick-Baez mirrors. The sample was placed onto a high-precision translational stage at 45° relative to the incident beam and raster scanned. XRF data was collected using a Vortex-EM XRF detector at a 20 μm × 20 μm resolution. Scanning was performed at a rate of 0.5 s/pixel. The emission lines of Cr, Fe, Ni, Ca, and Ti were used to determine crystal grain locations. Since the XRF detector is only sensitive in the 2000–20,000 eV range, Si (Kα = 1740 eV) and C (Kα = 277 eV) cannot directly be detected, so the SiC location was determined through the absence of any signals.

Microdiffraction mapping was performed on SiC1, SiC2, and SiC3 grains (Table 1), allowing some margin around each crystal to account for the penetration depth of the beam (~100 μm in SiC) and the 45° geometry of the sample relative to the incident beam. Data was collected in 90° geometry by a Pilatus 1M detector using a 0.5 s exposure time. The sample-to-detector distance was calibrated using an unstrained synthetic Si sample. Further information about the experimental setup can be found in Kunz et al. [45] and Stan et al. [46]. μXRD data analysis was performed using XMAS [45,47], the super-computing facilities at the National Energy Research Scientific Computing Center (NERSC).

Table 1. Measurement conditions for microdiffraction.

Grain	Map Dimensions (μm^2)	Pixel Dimension (μm)
SiC1	798 × 972	6
SiC2	1064 × 1080	8
SiC2 [a]	382 × 202	2
SiC3	665 × 755	5

[a] The second map was performed over the area where Si was present.

Raman maps of the Si inclusion in SiC2 were collected on a Horiba LabRam Evolution Raman spectrometer with a focal length of 800 mm. Spectra were collected from 450–900 cm^{-1} and the colors were assigned based on the first order Raman mode of Si and the manifold of TO modes for 4H- and 6H-SiC centered near 775 cm^{-1}. Spectra were collected in a backscattered geometry with an excitation wavelength of 532 nm and an 1800 lines/mm grating, which results in a spectral resolution of ~1 cm^{-1}. An Olympus BXFM-ILHS microscope with a 50× long working distance objective was used to focus the laser beam to a ~2 μm spot size onto the sample. Maps were collected using a 2 μm step size. A synthetic, unstrained Si chip was used to calibrate the Raman spectrometer. The peaks were fit using non-linear least squares to background-subtracted pseudo-Voight or Gaussian line profiles using the program Igor Pro (Version 8.0.4.2, WaveMetrics, Inc., Lake Oswego, OR, USA).

3. Results

Three grains of SiC (size ~0.5–1 mm) were chosen for detailed studies. XRF measurements corresponded well with the known shape and dimensions of each grain, as expected from optical microscope images of the sample (Figure 2).

3.1. SiC1

Initial μXRD measurements indicates that the sample consists of a strongly diffracting single crystal. Initial indexing attempts focused on the 4H-SiC polytype, which we anticipated based on previous TEM and Raman spectroscopic work [41]. Most of the scanned area could be indexed as either 4H- or 6H-SiC, with more than 30 peaks indexed for both polytypes (Figure 3). It is expected in general that 6H-SiC would have more diffraction peaks than 4H-SiC over the same angular range, due to the difference in the c-axis length between the two phases. This can easily be seen in the relative number of indexed peaks (Figure 3a,b).

The grain contains an area of overlap where both unit cells can be indexed (Figures 3 and 4). On the left-hand side of the grain, all observed peaks can be indexed as 4H-SiC only (Figure 4a), whereas on the right-hand side, all peaks can be indexed as 6H-SiC only (Figure 4c). In the center, the diffraction pattern contains peaks from both, and both can be indexed, with some peaks overlapping for both unit cells (Figure 4b).

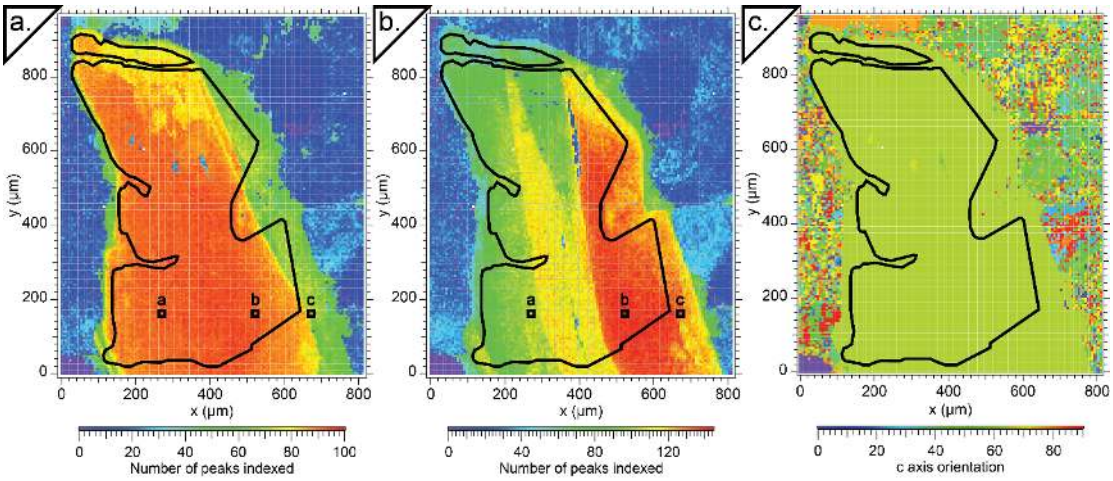

Figure 3. Grain can be indexed as both (**a**) 4H-SiC; and (**b**) 6H-SiC; (**c**) c-axis orientation with respect to the sample normal is also shown, to demonstrate the intergrowth of the two crystal types along the same stacking direction. The black outline indicates the surface expression of the sample, based on microscopy images. The squares labelled a, b, and c correspond to the diffraction pattern locations from Figure 4.

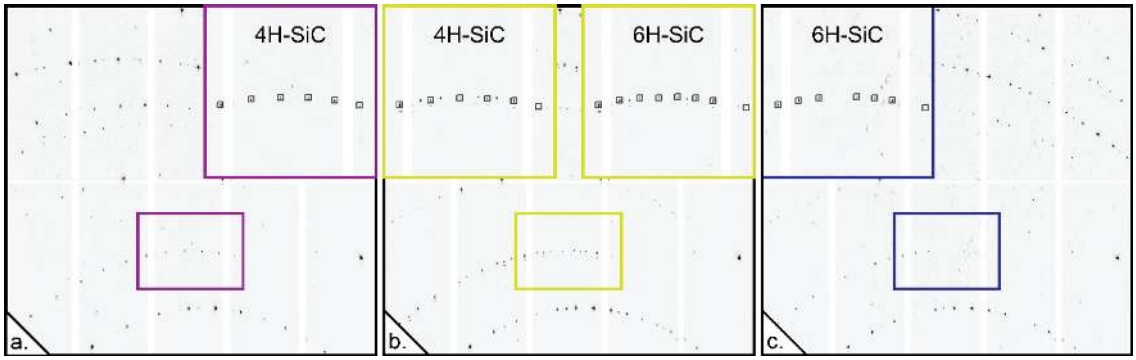

Figure 4. Diffraction patterns from SiC1 can be indexed as either the 4H- or 6H-SiC. (**a**). This part of the sample indexes solely as 4H-SiC. The inset shows squares around all successfully identified peaks. No additional peaks remain. (**b**). This area can be indexed as both 4H- and 6H-SiC. The two insets show that all peaks are identified as being part of one or the other stacking type. (**c**). This pattern can be fully indexed as 6H-SiC, as seen in the inset.

3.2. SiC2

The bulk of this grain consists of a strongly diffracting single crystal that indexes as 4H-SiC (Figure 5). The lower right-hand portion of the SiC2 sample contains both, the region where an Si inclusion was found, as well as a more poorly indexed region that is better fit as a 6H-SiC (Figure 5b). Although, a second Si inclusion was identified by optical microscopy and scanning electron microscopy (SEM) [41], the diffraction data were of insufficient quality to index it. We chose the mixed 4H/6H-SiC area for more detailed mapping and analyzed it with 2 µm × 2 µm resolution. The bulk 4H-SiC crystal pattern is visible in this entire area. However, single crystal diffraction, taking the form of continuous lines, can also be observed (Figure 6). We can fit the pattern using a 6H-SiC unit cell, which provides a more accurate fit than the 4H-SiC pattern of the rest of the crystal body. This can be seen when comparing Figure 6e,f, where all maxima can be captured with a 6H-SiC fit except for a select few, which correspond to 4H-SiC. However, most of the grain is polycrystalline in this area, with a few discrete orientations dominating (Figure 5c).

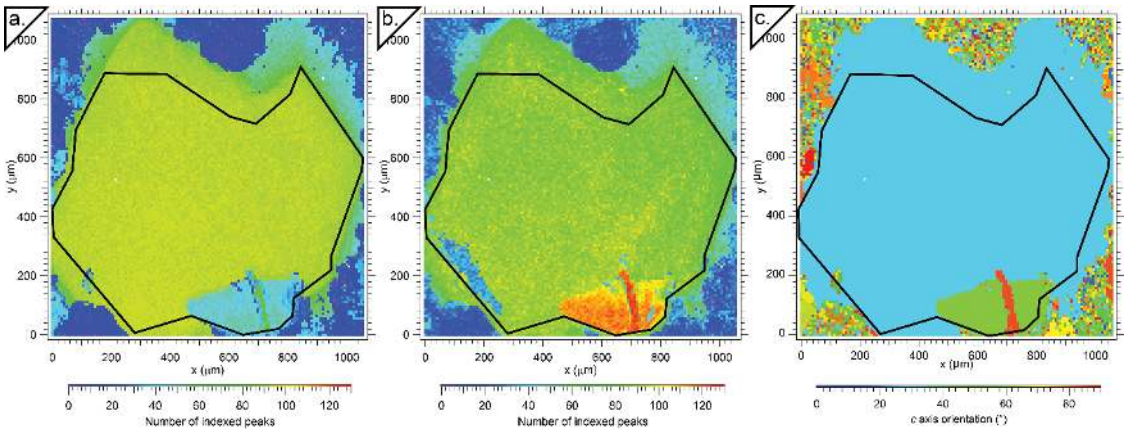

Figure 5. The SiC2 grain indexed as (**a**). 4H-SiC and (**b**). 6H-SiC. (**c**). The c-axis orientation with respect to the sample normal shows several different orientations are present in this sample. The black outline indicates the surface expression of the sample, based on microscopy images.

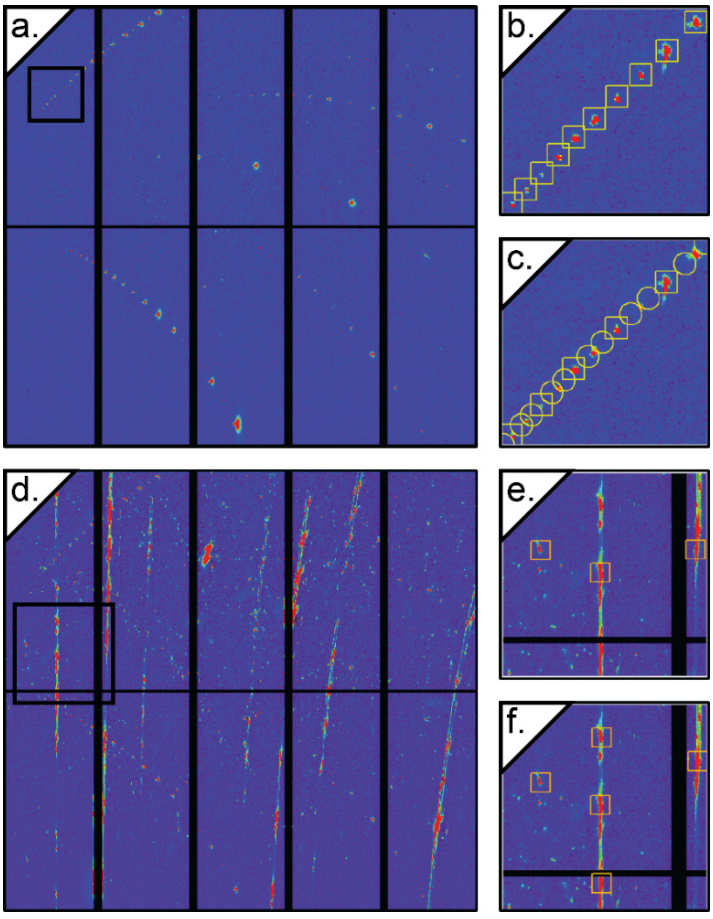

Figure 6. (**a**). This pattern is representative of the SiC2 sample in the 4H-SiC-indexed region. (**b**). The yellow squares indicate peaks that were identified and indexed as 4H-SiC. All peaks can be fit with this unit cell. (**c**). The same pattern from a. is indexed as 6H-SiC. The yellow circles show peaks that are predicted to occur, but are not found (with signal-to-noise ratio > 5). (**d**). This pattern is representative of the polycrystalline region of the SiC2 sample (**e**) and (**f**). are representative fits to the 4H- and 6H-SiC unit cells, respectively. Boxes in (**a**). and (**d**). outline enlarged areas from (**b**)., (**c**)., (**e**) and (**f**).

A native Si inclusion was initially identified by visual inspection due to differences in its reflectivity relative to the surrounding SiC. This inclusion occurs within the mixed 4H-/6H-SiC region of the

sample. By scanning through the diffraction patterns, we find one area with broad, deformed peaks (Figure 7) that can be indexed as diamond structured ($Fd\bar{3}m$) Si. At least 3 distinct crystallographic orientations can be indexed, indicating that the native Si inclusion is polycrystalline, but with large grain sizes (Figure 7b–d). These grains overlap for some part of the sample. A {113} reflection is the most intense in all three crystallites. Examination of this peak, however, indicates that it is likely that many more subgrains exist, as evidenced by the existence of several overlapping maxima (Figure 7e–g). This is also indicative of a plastic deformation that is significant enough to cause a subgrain boundary formation. Although, an area of only ~36 µm × ~30 µm is exposed to the surface, we can track the persistence of the {113} reflection in these three main Si grains for at least 340 µm horizontally and 590 µm vertically. This area of persistence is roughly coincident with where 6H-SiC is present, but with inhomogeneous diffraction intensity suggesting varying emplacement depths and/or grain thickness in Si.

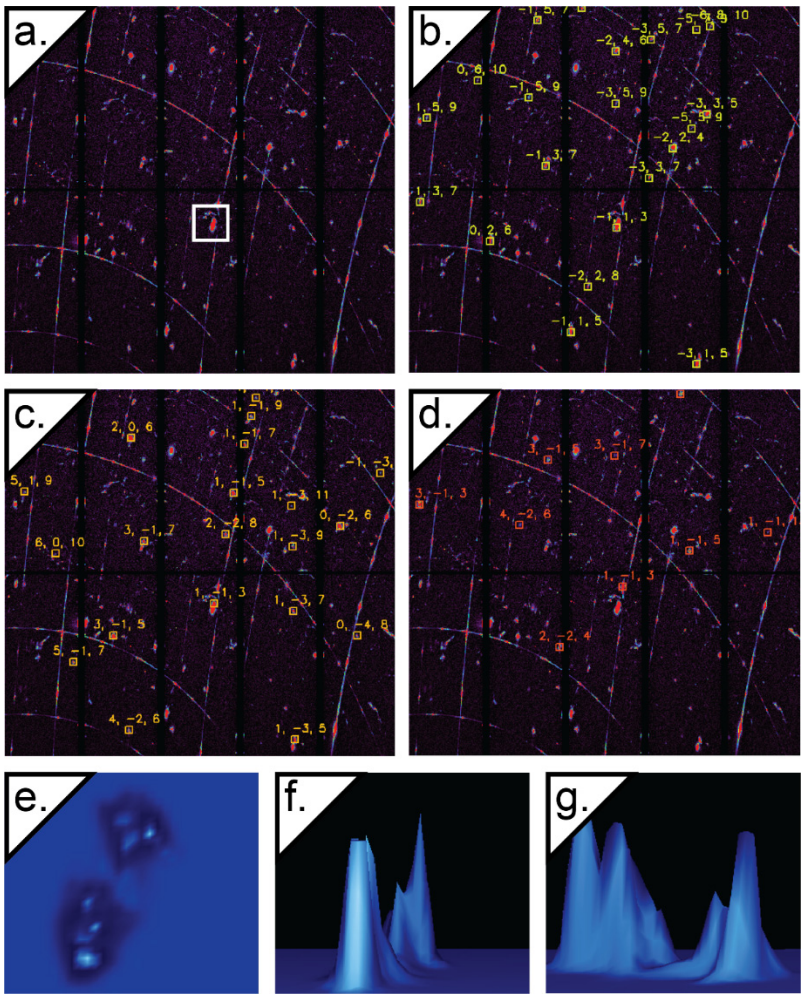

Figure 7. (**a**). This is a representative pattern taken in the region of exposed Si inclusion. (**b**)., (**c**)., and (**d**). show indexation fits for three different Si orientations (~33.5, 15.5, and 24.8° *c*-axis orientation with respect to sample normal, respectively). (**e**). This is a magnified view of the {113} reflection outlined by a white box in (**a**,**f**). and (**g**). show three-dimensional (3D) projections of the peaks from e. in vertical, and horizontal transects, respectively.

A Raman map of the Si inclusion is shown in Figure 8. The 4H- and 6H-SiC can also be identified from the Raman spectra, but were not the focus of this measurement. The single Raman mode of silicon is due to the first-order Raman scattering of the longitudinal optical (LO) and the transverse optical (TO) phonon modes, which are degenerated at the Γ-point [48]. Its room pressure and temperature

position has been reported to range from 519.5 ± 0.8 cm^{-1} to 523.0 ± 1.0 cm^{-1} [49–52]. The large range of reported frequencies is likely due to many factors, such as instrument calibration, tensile, or compressive stress state of the Si sample. More recently it has been shown that the Raman mode of un-stressed Si is observed between 520.5 and 520.7 cm^{-1} [48,53]. In this sample, the Si Raman mode ranges from 522.3 to 525.2 cm^{-1}.

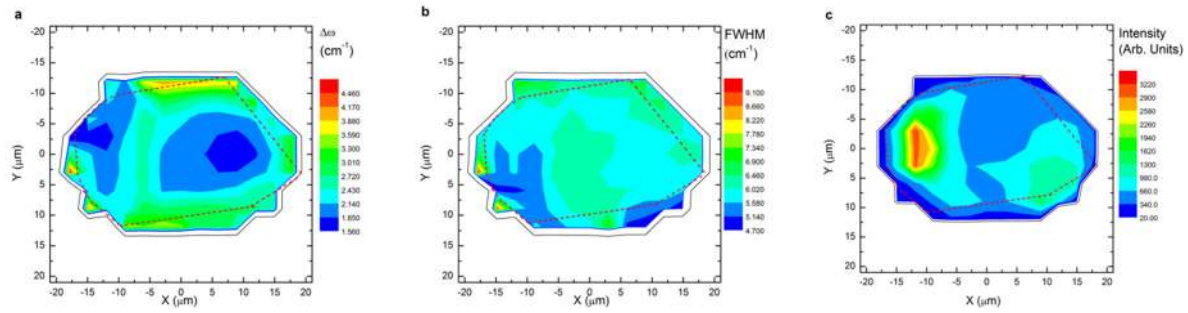

Figure 8. Raman maps of the Si inclusion. (**a**). $\Delta\omega = \omega_{observed} - \omega_{unstrained\ Si.}$ a value of 520.7 cm^{-1} was used for the unstrained Si. (**b**). Full width at half maximum (FWHM) of the first order Si Raman mode. (**c**). Intensity of the first order Si Raman mode. The red dashed line outlines the surface expression of the Si inclusion.

3.3. SiC3

Like SiC1, the SiC3 grain is made of two overlapping domains, which easily index to 4H-SiC or 6H-SiC (Figure 9). The overlap region is like that of SiC1 (Figure 4), where peaks from both orientations can be observed, suggesting that the two structures are intercalated. A second SiC orientation is observed on the left-hand side of the grain, which visually appears to coincide with the presence of both a slight fracture in the grain as well as the presence of a metal silicide inclusion [41]. The data were insufficient to determine the mineral type of the silicide.

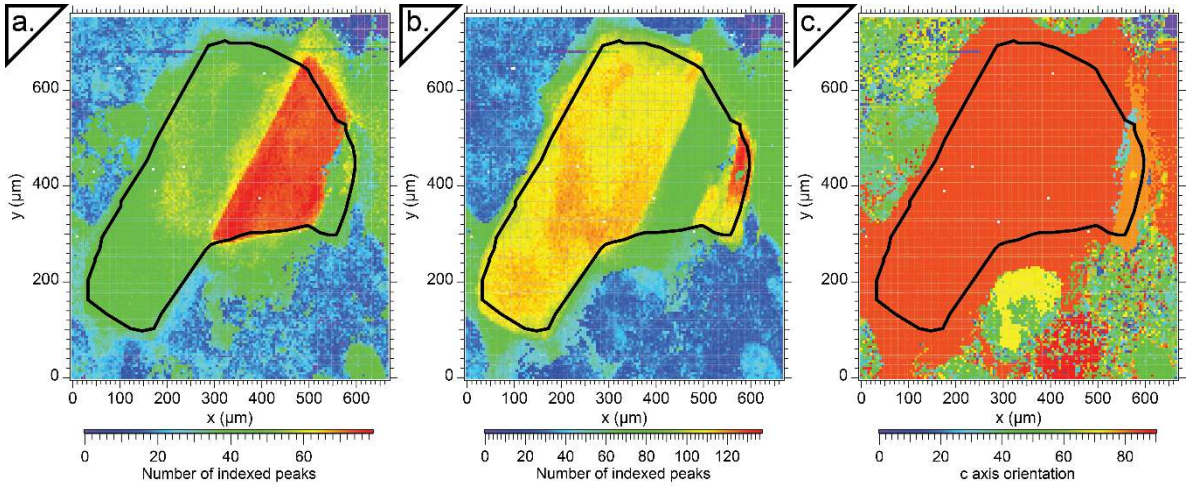

Figure 9. The SiC3 grain indexed as (**a**). 6H-SiC and (**b**). 4H-SiC. (**c**). The c-axis orientation with respect to the sample normal shows several different orientations are present in this sample. The black outline indicates the surface expression of the sample, based on microscopy images.

4. Discussion

4.1. SiC Formation—Geological Context

The three crystals of SiC in the studied sample are characterized as xenocrysts transported together with other pyroclastic materials by the volcanic vent related to Miocene intraplate alkali

basalt activities [41]. Together with other pyroclastic materials, they mixed with ashes and local sediments containing microfauna (Figure S1) to become a part of the tuffite/tuffo-sandstone formation. Dobrzhinetskaya et al. [41] hypothesized that SiC, presented in the 4H-SiC and 6H-SiC polytypes, was formed at depth ~60–100 km, through the reaction of SiO_2 (melt) with highly reducing fluids (H_2O–CH_4–H_2–C_2H_6, as proposed by Zhang and Duan, [54]). This is supported by well-known reactions which could assist the formation of both SiC and Si:

$$SiO_2\ (melt) + CH_4 \rightarrow SiC + 2H_2O \quad (1)$$

$$2CH_4 + H_2O \rightarrow 4H_2 + 2CO \rightarrow C + CO_2 + 4H_2 \quad (2)$$

$$SiO_2 + C \rightarrow Si + CO_2 \quad (3)$$

According to Dobrzhinetskaya et al. [41], the ultra-reduced fluid, originating from a mantle hot spot, could pass through an alkaline basalt magma reservoir and interact with the SiO_2 available from the walls of the crustal rocks surrounding this magmatic reservoir. This would lead to the formation of SiC, and this process could be accompanied by the reduction of metal-oxides to native metals, alloys, and silicides that could have originated from droplets of an immiscible melt fraction trapped by SiC during its crystallization.

4.2. Stress/Strain Relationships and Crystal Grain Formation

The three SiC grains fall into two distinct categories, based on the spatial distribution of the 4H- and 6H- unit cells. In the case of SiC1 and SiC3, there is an orientational relationship between the 4H- and 6H-SiC regions, where both unit cells can be described by the same orientation matrix. By traversing a sample, we can observe a 4H-SiC region, a mixed region where some lattice planes are shared, and finally a 6H-SiC region. The intercalation and lack of reorientation suggests that the sample is a single grain. Studies suggest that the degree of hexagonality of SiC varies with the Si/C ratio (Haase et al. [6] and references contained therein). Therefore, grains with variable structure, such as SiC1 and SiC3, could have grown from a slowly cooling Si/C melt slightly enriched in Si, where SiC growth would have led to C depletion in the melt and an increased Si/C ratio. In such a scenario, 4H-SiC would be formed at first, and continuous grain growth would lead to a less hexagonal (containing some cubic ABC stacking planes) structure over time as the surrounding melt changed, explaining the transition region between the two crystal types and the final 6H-SiC structure.

In the case of SiC2, there is no such relationship in the orientation of 4H-SiC and 6H-SiC, nor between SiC and Si. It is more likely that the 4H-SiC grain, which is visible in the diffraction patterns where 6H-SiC is also present, formed independently during different melting events from the 6H-SiC, and that these single crystals became intergrown or cemented together by remaining liquid Si at a later time.

The differential stress and strain in both SiC and Si were calculated from the indexed Laue diffraction map. In the 4H-SiC region, the stress/strain across the crystal was homogeneous for a given tensor, so we focus the discussion mainly on the part of the map that covers the exposed Si region and the entire 6H-SiC region. The strain in this area for all 3 crystal types is presented in Figure 10a–c. The overall strain in the 4H-SiC region of the sample is low, except for some tensile differential strain in the z direction of the sample; this observation may be due to the release of pressure as a result of cutting and polishing the sample. The Si is under compressive differential strain in the XY plane and tensile differential strain in the Z direction. The strain state seems not to depend on the crystallographic orientation of any of the 3 phases.

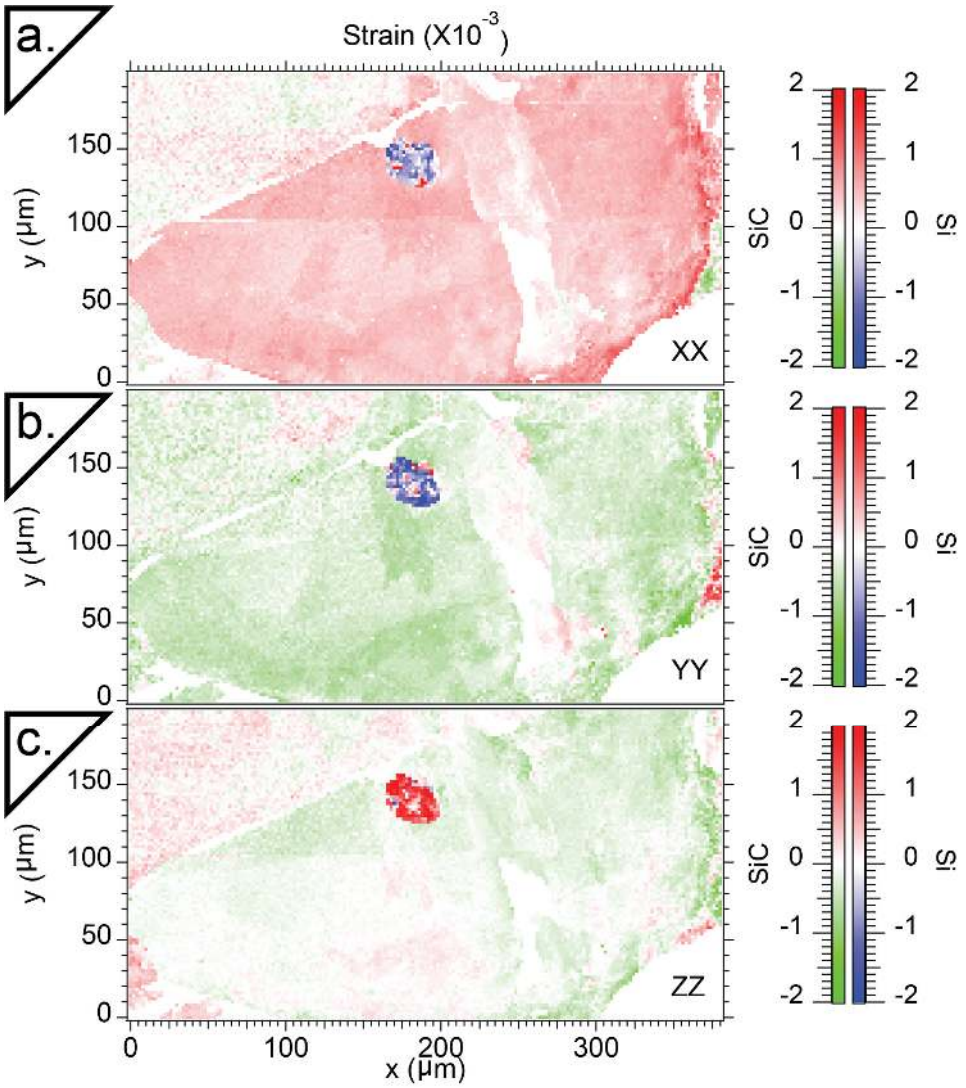

Figure 10. Strain maps of the mixed 4H-/6H-SiC region and Si inclusion in the (**a**) x (horizontal) (**b**) y (vertical) and (**c**) z (out of plane) directions.

A possible explanation for this may be that greater plastic deformation and differential strain in Si is due to a differential in the coefficient of thermal expansion (CTE) for the two materials, where SiC = 4.36×10^{-6} K^{-1} [55] and Si = 2.63×10^{-6} K^{-1} [56]. In prior studies of dislocation generation between materials with contrasting CTE, it was found that the dislocation density increased relative to the pure materials when subjected to similar temperature conditions [57,58]. We assume that the Si inclusion formed while the sample was at high temperature, which is reasonable as this SiC sample likely formed at a depth of 60–100 km (~2 GPa) and a temperature range of 1000–1600 °C [41]. Then the factor of ~2 differences in their CTE is likely the cause of the higher dislocation densities associated with the Si and SiC in the 6H-SiC region. In essence, SiC would contract at a faster rate than Si, leading to greater strain in the Si. We map the dislocation densities in both, assuming a {001}<110> slip system in SiC (Figure 11). This assumption is borne out by the presence of diffraction "lines" in the single-crystal Laue diffraction of SiC, which are indicative of stacking faults and are direct evidence of the activation of this slip system. Overall, Si displays a much greater density of dislocations than SiC. This is supported by observations in the diffraction, which suggest that the Si is under more plastic deformation at every point where both are present.

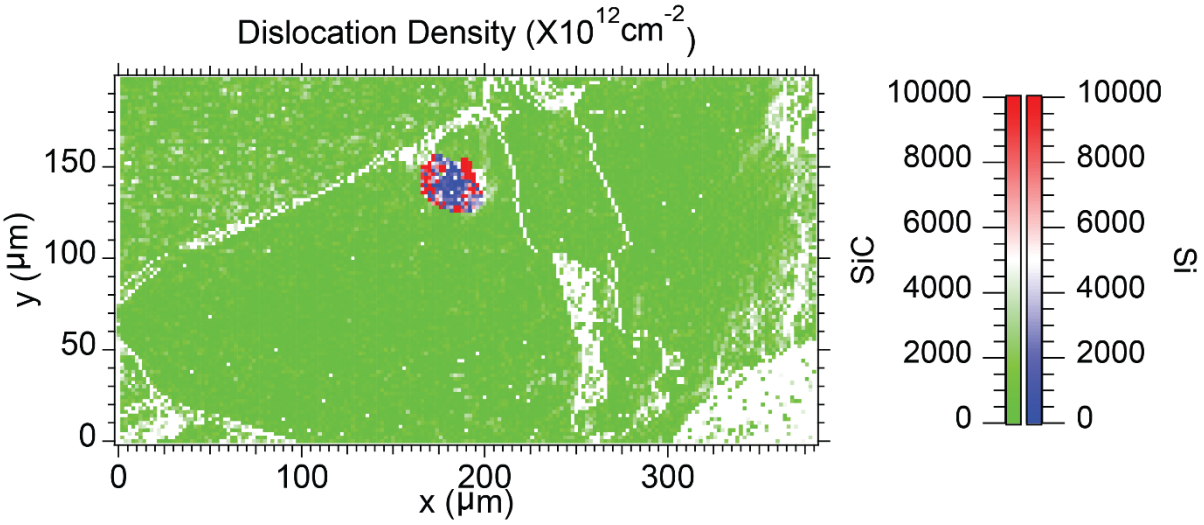

Figure 11. Geometrically necessary dislocation density of the mixed 4H-/6H-SiC region and Si inclusion. Notably the dislocation density of the Si inclusion is high at the edges and low in the middle and the SiC grain shows a very low dislocation density.

4.3. SiC/Si Relationship

One of the goals of our study was to understand the formation of a native silicon inclusion, such as that found in SiC2, which requires extremely reducing conditions of formation [21]. Due to the wide use of silicon in the semiconductor industry the effects of tensile and compressive stresses, hydrostatic pressure, temperature, and polishing on the first order Raman mode position and width are well-characterized [48,50,52,53,59–66]. It is well-known that tensile and compressive stress affect the Raman line by a redshift, and blueshift, respectively [61,62]. Anastassakis et al. [59] reported a splitting of the first order Raman mode of Si under uniaxial stress along the [001] or [111] direction. Thus, the observed shift in the first order Raman mode of our Si inclusion (Figure 8a) may be evidence of residual compressive stress. Most of the grain shows a shift of ~1.5–2.7 cm^{-1} (Figure 8a) from the ambient pressure value of 520.7 cm^{-1}. Taking the pressure shift of the first order Si Raman mode reported by Weinstein and Piermarini [52] this could suggest that the Si grain records a residual pressure of ~0.3–0.5 GPa.

The FWHM of this peak ranges from ~4–9 cm^{-1} (Figure 8b). The room pressure and temperature FWHM of unstrained Si has previously been reported to range from ~3.2–7.0 cm^{-1} depending on the laser power [50,60,63,64]. Fitting very low intensity modes can be difficult and can result in larger errors in peak position and FWHM. However, even disregarding the very large and small observed FWHMs, the majority of the Raman spectra of the Si inclusion have FWHM of ~5.5–7.7 cm^{-1}. Weinstein and Piermarini [52] report that there is no appreciable change in the peak shape with applied pressure to ~10 GPa. Hence, our observed peak widths and shapes did not unambiguously indicate that our inclusion recorded any residual pressure.

Not surprisingly, the largest mode shifts are observed near the edge of the Si inclusion, and the smallest shifts near the center of the inclusion. These shifts also correspond to regions of largest FWHM and lowest intensity (Figure 8c). We also observe some asymmetry to the higher wave-number side of the observed Si Raman modes primarily in the spectra collected near the edge of the Si inclusion, suggesting a uniaxial component to the residual stress. This is consistent with the diffraction measurements discussed above, where plastic deformation was clearly observed as asymmetrical streaking in three-dimensional (3D) peak shape (Figure 7e–g). Furthermore, a lower Raman intensity is observed at the edges of the inclusion, which can be explained by considering the penetration depth of the Raman measurements. The penetration depth of a laser is dependent on the material absorption coefficient, α, which is wavelength- and temperature-dependent, but for a constant α, intensity decays

exponentially with depth, according to the Beer-Lambert Law. For a 532 nm laser the penetration depth in Si is ~0.7 μm [67]. The lowest intensities are from just outside where the Si inclusion is exposed to the surface, and these spectra also show peaks that are from SiC (Figure 8c).

Nazzareni et al. [43] report natural SiC from a peralkaline syenite from the Azores. They identified an Si inclusion with Raman spectroscopy and report that the first order Raman mode of Si was observed to be at 519.65 cm^{-1}, and the position of the synthetic Si first order Raman mode is 520.72 cm^{-1}. As discussed above and by Nazzareni et al. [43], the residual pressure of the Si inclusion was calculated using the pressure shift of the first order Raman mode of Si, reported by Weinstein and Piermarini [52]. In contrast to our results, Nazzareni et al. [43] report that the first order Raman mode of their Si inclusion is observed to be lower than the ambient pressure value, suggesting that it records a negative residual pressure. It should be noted that, in the absence of a detailed compositional analysis of the Si inclusion, reported by Nazzareni et al. [43], the negative shift could be due to impurities such as Fe, which, for example, has been reported in native silicon from the Luobusa Ophiolite [68]. Much of our Si inclusion is still enclosed within SiC, and only the upper part of the inclusion was exposed to the surface during cutting. Therefore, we can hypothesize that the positive shift of the Raman mode of our Si inclusion probably reflects some residual pressure similar but opposite to the conclusions reached by Nazzareni et al. [43].

A considerable amount of work has been reported on subsurface damage in Si, due to polishing and grinding [66,69]. It is possible that our observed shift in the first order Si Raman mode is a result of damage caused during sample polishing. Shifts of ~1 cm^{-1} are observed in the core of the exposed Si inclusion while larger shifts are observed at the edge of the exposed inclusion. Zhang et al. [66] report that the position of the first order Si Raman mode for several Si wafers that were polished with different grain sizes ranging from ~70–~4 μm. The ground wafer surfaces mainly present compressive states that are dependent on the grain sized used for polishing and shifts up to 4 cm^{-1} from the ambient value are observed. The main reason for the generation of residual stresses is due to phase transitions. Zarudi and Zhang [69] discuss subsurface damage of single-crystal silicon due to grinding and polishing. They show that the depth of damage is related to the particle size of the abrasives used, and that the damage can be removed with polishing (about 10 h). Phase transitions to α-Si, Si-III, and Si-XII are also observed in polished Si samples and the phases that are observed is dependent on the grain size of the polish that was used [66]. We do not observe any peaks from α-Si, Si-III, or Si-XII in our spectra. The stress regime in the near-surface environment of the polished and exposed Si inclusion isn't simple, and likely grades from mostly compressive near the edges to more tensile in the middle. It is difficult to deconvolve the signals from, (1) actual residual pressure that may be recorded by the grain, due to thermal expansion differences, (2) artefacts from polishing the sample, and (3) the exposure of the Si inclusion to the surface on one side. To verify these statements, it will be necessary to conduct additional Raman experiments of synthetic Si crystals before, and after, polishing.

5. Conclusions

We performed μXRD and Raman spectroscopy studies of three grains of natural SiC and found that each of them consists of two polytypes of SiC, 4H- and 6H-SiC. These SiC polytypes were found to be either, intergrown during a single growth event (SiC1 and SiC3), or cemented together after the initial formation of SiC crystals (SiC2) with polycrystalline, more deformed Si. There is no straightforward explanation for which SiC polytype will form first, and current theories, include impurity arguments, kinetic, and growth considerations, as well as thermodynamics. In a natural system the liquid will have a particular Si/C ratio, as well as some quantity of impurities. This liquid will cool at some rate and a certain SiC polytype will crystallize. Since we observe both 4H- and 6H-SiC, and if we assume a closed system crystallization of SiC, crystal growth will change the Si/C ratio. It has been proposed that the Si/C ratio will determine which type of polytype will form [6]. This hypothesis aims to explain the natural zoned SiC that was found in metamorphic rocks from Bulgaria [42]. Thus, we propose that for SiC1 and SiC3 one nucleation event led to grain formation through a change in the Si/C ratio, likely

caused by C depletion during grain growth, and in the case of SiC2 two different nucleation events likely occurred.

Despite its high hardness, SiC deforms plastically and polygonizes at a high temperature [70]. Dislocations in (0001), dislocations with $\left[1\bar{1}20\right]$ vectors, pileups formed by slip, and dislocation walls formed by climb, were all reported by Amelinckx et al. [70]. Dislocations in microdiamonds have also been reported [71,72]. Kvasnytsya and Wirth [72] report a high density of curved dislocations in one of their microdiamond samples from a meteorite impact area and suggest a thermally activated process where the diamond experienced a period of thermal annealing after deformation. Dobrzhinetskaya et al. [71] found dislocations in microdiamonds from ultra-high-pressure metamorphic terranes and assigned them to dislocations of growth, e.g., during the nucleation process, the volume may have been under differential stress. The observed low dislocation density in the examined SiC crystals suggests that the samples may not have remained at high temperatures for an extended period, nor did they undergo any high temperature deformation at any time after their initial crystallization. While these new results still cannot place any constraint on the depth of formation of these grains, they do support their high-temperature origin which was reported earlier by Dobrzhinetskaya et al. [41]. Given the wide stability field of SiC, from the shallow mantle to the deep Earth, one should be cautious when interpreting formation conditions of natural SiC.

Supplementary Materials: The following are available online at http://www.mdpi.com/2075-163X/10/3/204/s1, Figure S1: (**a**). Optical microscope image of the tuffite sample containing 3 SiC crystals. The red outline indicates the location of the microfossil/microfauna. (**b**). Microfossil/microfauna as seen at larger magnification.

Author Contributions: C.V.S., E.F.O.III, data collection and interpretation, writing, and editing; N.T., data collection and interpretation; P.M., resources and sample preparation; L.D., conception, data interpretation, writing, and editing. All authors have read and agreed to the published version of the manuscript.

Funding: EFO was partially supported by NSF through EAR-1620423 and acknowledges helpful discussions with Q. Williams UCSC. A portion of this work was performed under the auspices of the US Department of Energy by Lawrence Livermore National Laboratory under Contract No. DE-AC52-07NA27344. This research used resources of the National Energy Research Scientific Computing Center, a DOE Office of Science User Facility supported by the Office of Science of the U.S. Department of Energy under Contract No. DE-AC02-05CH11231. The Advanced Light Source is supported by the Director, Office of Science, Office of Basic Energy Sciences, Materials Sciences Division, of the U.S. Department of Energy under Contract No. DE-AC02-05CH11231 at Lawrence Berkeley National Laboratory and University of California, Berkeley, California.

Conflicts of Interest: The authors declare no conflict of interest.

References

1. Cheung, R. *Silicon Carbide Microelectromechanical Systems for Harsh Environments*; Imperial College Press: London, UK, 2006; ISBN 978-1-86094-624-0.
2. Ramsdell, L.S. Studies on silicon carbide. *Am. Mineral.* **1947**, *32*, 64–82.
3. Jepps, N.W.; Page, T.F. Polytypic transformations in silicon carbide. *Prog. Cryst. Growth Charact.* **1983**, *7*, 259–307. [CrossRef]
4. Powell, J.A.; Will, H.A. Low-temperature solid-state phase transformations in 2H silicon carbide. *J. Appl. Phys.* **1972**, *43*, 1400–1408. [CrossRef]
5. Jagodzinski, H. Polytypism in SiC crystals. *Acta Cryst.* **1954**, *7*, 300. [CrossRef]
6. Haase, V.; Kirschstein, G.; List, H.; Ruprecht, S.; Sangster, R.; Schröder, F.; Töpper, W.; Vanecek, H.; Heit, W.; Schlichting, J.; et al. *Si Silicon: System Si-C. SiC: Natural Occurrence. Preparation and Manufacturing Chemistry. Special Forms. Manufacture. Electrochemical Properties. Chemical Reactions. Applications. Ternary and Higher Systems with Si and C*; Gmelin Handbook of Inorganic Chemistry; Springer-Verlag Berlin Heidelberg: Berlin, Germany, 1985; Volume B3, ISBN 978-3-662-06994-3.
7. Burdick, C.L.; Owen, E.A. The structure of carborundum determined by X-rays. *J. Am. Chem. Soc.* **1918**, *40*, 1749–1759. [CrossRef]
8. Thibault, N.W. Morphological and structural crystallography and optical properties of silicon carbide (SiC). *Am. Mineral.* **1944**, *29*, 327–362.
9. Moissan, H. Nouvelles recherches sur la météorité de Cañon Diablo. *Comptes rendus* **1904**, *139*, 773–786.

10. Milton, C.; Vitaliano, D.B. Moissanite SiC, a geological aberration. In Proceedings of the 98th Annual Meeting of the Geological Society of America, Orlando, FL, USA, 14 October 1985; p. 665.
11. Abderrazak, H.; Hmida, E.S.B.H. Silicon Carbide: Synthesis and Properties. In *Properties and Applications of Silicon Carbide*; InTech: Rijeka, Croatia, 2011; p. 361.
12. Lyakhovich, V.V. Origin of accessory moissanite. *Int. Geol. Rev.* **1980**, *22*, 961–970. [CrossRef]
13. Marshintsev, V.K. Nature of silicon carbide in kimberlite rocks of Yakutiya. *Mineral. Zhurnal* **1990**, *12*, 17–26.
14. Leung, I.; Guo, W.; Friedman, I.; Gleason, J. Natural occurrence of silicon carbide in a diamondiferous kimberlite from Fuxian. *Nature* **1990**, *346*, 352. [CrossRef]
15. Qi, X.; Yang, J.; Xu, Z.; Bai, W.; Zhang, Z.; Fang, Q. Discovery of moissanite in retrogressive eclogite from the Pre-pilot Hole of the Chinese Continental Scientific Drilling Project (CCSD-PP2) and its geological implication. *Acta Petrol. Sin.* **2007**, *23*, 3207–3214.
16. Lee, J.-S.; Yu, S.-C.; Tung, S.-F.; Bai, W.-J.; Yang, J.-S.; Fang, Q.-S.; Zhang, Z. The crystal structure of natural 33R moissanite from Tibet. *Z. für Krist.–Cryst. Mater.* **2009**, *221*, 213–217. [CrossRef]
17. Kaminsky, F. Mineralogy of the lower mantle: A review of 'super-deep' mineral inclusions in diamond. *Earth-Sci. Rev.* **2012**, *110*, 127–147. [CrossRef]
18. Shiryaev, A.A.; Griffin, W.L.; Stoyanov, E. Moissanite (SiC) from kimberlites: Polytypes, trace elements, inclusions and speculations on origin. *Lithos* **2011**, *122*, 152–164. [CrossRef]
19. Ballhaus, C.; Wirth, R.; Fonseca, R.O.C.; Blanchard, H.; Pröll, W.; Bragagni, A.; Nagel, T.; Schreiber, A.; Dittrich, S.; Thome, V.; et al. Ultra-high pressure and ultra-reduced minerals in ophiolites may form by lightning strikes. *Geochem. Perspect. Lett.* **2017**, *5*, 42–46. [CrossRef]
20. Ballhaus, C.; Blanchard, H.; Fonseca, R.O.C.; Bragagni, A. Reply 2 to Comment on "Ultra-high pressure and ultra-reduced minerals in ophiolites may form by lightning strikes". *Geochem. Perspect. Lett.* **2018**, *8*, 8–10. [CrossRef]
21. Mathez, E.A.; Fogel, R.A.; Hutcheon, I.D.; Marshintsev, V.K. Carbon isotopic composition and origin of SiC from kimberlites of Yakutia, Russia. *Geochim. Cosmochim. Ac.* **1995**, *59*, 781–791. [CrossRef]
22. Golubkova, A.; Schmidt, M.W.; Connolly, J.A.D. Ultra-reducing conditions in average mantle peridotites and in podiform chromitites: a thermodynamic model for moissanite (SiC) formation. *Contrib. Mineral. Petrol.* **2016**, *171*, 41. [CrossRef]
23. Ohrenschall, R.D.; Milton, C. The occurrence of moissanite (silicon carbide) in sediments. *J. Sediment. Res.* **1931**, *1*, 96–99.
24. Kaminskiy, F.V.; Bukin, V.J.; Potapov, S.V.; Arkus, N.G.; Ivanova, V.G. Discoveries of silicon carbide under natural conditions and their genetic importance. *Int. Geol. Rev.* **1969**, *11*, 561–569. [CrossRef]
25. Ross, J. *Kimberlites and Related Rocks*; John Wiley & Sons: Hoboken, NJ, USA, 1989; ISBN 978-0-86793-384-0.
26. Leung, I.S. Silicon carbide cluster entrapped in a diamond from Fuxian, China. *Am. Mineral.* **1990**, *75*, 1110–1119.
27. Wilding, M.C.; Harte, B.; Harris, J.W. Evidence for a deep origin of São Luis diamonds. In *CPRM Special Publication 2/91, Proceedings of the Extended Abstracts 5th International Kimberlite Conference*; CPRM: Brasília, Brazil, 1991; pp. 456–458.
28. Svisero, D.P. Distribution and origin of diamonds in Brazil: An overview. *J. Geodyn.* **1995**, *20*, 493–514. [CrossRef]
29. Di Pierro, S.; Gnos, E.; Grobety, B.H.; Armbruster, T.; Bernasconi, S.M.; Ulmer, P. Letters. Rock-forming moissanite (natural α-silicon carbide). *Am. Mineral.* **2003**, *88*, 1817–1821. [CrossRef]
30. Zhang, Z. Native gold and native copper grains enclosed by olivine phenocrysts in a picrite lava of the Emeishan large igneous province, SW China. *Am. Mineral.* **2006**, *91*, 1178–1183. [CrossRef]
31. Klein-BenDavid, O.; Wirth, R.; Navon, O. Micrometer-scale cavities in fibrous and cloudy diamonds—A glance into diamond dissolution events. *Earth Planet Sc. Lett.* **2007**, *264*, 89–103. [CrossRef]
32. Xu, S.; Wu, W.; Xiao, W.; Yang, J.; Chen, J.; Ji, S.; Liu, Y. Moissanite in serpentinite from the Dabie Mountains in China. *Mineral. Mag.* **2008**, *72*, 899–908. [CrossRef]
33. Trumbull, R.B.; Yang, J.-S.; Robinson, P.T.; Di Pierro, S.; Vennemann, T.; Wiedenbeck, M. The carbon isotope composition of natural SiC (moissanite) from the Earth's mantle: New discoveries from ophiolites. *Lithos* **2009**, *113*, 612–620. [CrossRef]
34. Yusupov, R.G.; Stanley, C.J.; Welch, M.D.; Spratt, J.; Cressey, G.; Rumsey, M.S.; Seltmann, R.; Igamberdiev, E. Mavlyanovite, Mn5Si3: A new mineral species from a lamproite diatreme, Chatkal Ridge, Uzbekistan. *Mineral. Mag.* **2009**, *73*, 43–50. [CrossRef]

35. Fritsch, E.; Toledo, V.; Matlins, A. Record-size natural moissanite crystals discovered in Israel. *Gems Gemol.* **2014**, *50*, 160–161.
36. Liang, F.; Xu, Z.; Zhao, J. In-situ moissanite in dunite: deep mantle origin of mantle peridotite in Luobusa ophiolite, Tibet. *Acta Geol. Sin. Engl. Ed.* **2014**, *88*, 517–529. [CrossRef]
37. Liu, Y.; He, D.; Gao, C.; Foley, S.; Gao, S.; Hu, Z.; Zong, K.; Chen, H. First direct evidence of sedimentary carbonate recycling in subduction-related xenoliths. *Sci. Rep.* **2015**, *5*, 11547. [CrossRef] [PubMed]
38. Xu, X.; Yang, J.; Robinson, P.T.; Xiong, F.; Ba, D.; Guo, G. Origin of ultrahigh pressure and highly reduced minerals in podiform chromitites and associated mantle peridotites of the Luobusa ophiolite, Tibet. *Gondwana Res.* **2015**, *27*, 686–700. [CrossRef]
39. Yang, J.; Meng, F.; Xu, X.; Robinson, P.T.; Dilek, Y.; Makeyev, A.B.; Wirth, R.; Wiedenbeck, M.; Cliff, J. Diamonds, native elements and metal alloys from chromitites of the Ray-Iz ophiolite of the Polar Urals. *Gondwana Res.* **2015**, *27*, 459–485. [CrossRef]
40. Di Pierro, S.; Gnos, E. Ca-Al-silicate inclusions in natural moissanite (SiC). *Am. Mineral.* **2016**, *101*, 71–81. [CrossRef]
41. Dobrzhinetskaya, L.; Mukhin, P.; Wang, Q.; Wirth, R.; O'Bannon, E.; Zhao, W.; Eppelbaum, L.; Sokhonchuk, T. Moissanite (SiC) with metal-silicide and silicon inclusions from tuff of Israel: Raman spectroscopy and electron microscope studies. *Lithos* **2018**, *310–311*, 355–368. [CrossRef]
42. Machev, P.; O'Bannon, E.F.; Bozhilov, K.N.; Wang, Q.; Dobrzhinetskaya, L. Not all moissanites are created equal: New constraints on moissanite from metamorphic rocks of Bulgaria. *Earth Planet. Sci. Lett.* **2018**, *498*, 387–396. [CrossRef]
43. Nazzareni, S.; Nestola, F.; Zanon, V.; Bindi, L.; Scricciolo, E.; Petrelli, M.; Zanatta, M.; Mariotto, G.; Giuli, G. Discovery of moissanite in a peralkaline syenite from the Azores Islands. *Lithos* **2019**, *324–325*, 68–73. [CrossRef]
44. Baer, G.; Aharon, L.; Heimann, A.; Shaliv, G.; Agnon, A. The Nahal Tavor vent: Interplay of Miocene tectonics, dikes, and volcanism in the Lower Galilee, Israel. *Isr. J. Earth Sci.* **2006**, *55*, 1–16. [CrossRef]
45. Kunz, M.; Tamura, N.; Chen, K.; MacDowell, A.A.; Celestre, R.S.; Church, M.M.; Fakra, S.; Domning, E.E.; Glossinger, J.M.; Kirschman, J.L.; et al. A dedicated superbend X-ray microdiffraction beamline for materials, geo-, and environmental sciences at the advanced light source. *Rev. Sci. Instrum.* **2009**, *80*, 035108. [CrossRef]
46. Stan, C.V.; Tamura, N. Synchrotron X-ray Microdiffraction and Fluorescence Imaging of Mineral and Rock Samples. *JoVE* **2018**, in press. [CrossRef]
47. Tamura, N.; MacDowell, A.A.; Spolenak, R.; Valek, B.C.; Bravman, J.C.; Brown, W.L.; Celestre, R.S.; Padmore, H.A.; Batterman, B.W.; Patel, J.R. Scanning X-ray microdiffraction with submicrometer white beam for strain/stress and orientation mapping in thin films. *J. Synchrotron Radiat.* **2003**, *10*, 137–143. [CrossRef]
48. Merlen, A.; Sangar, A.; Torchio, P.; Kallepalli, L.N.D.; Grojo, D.; Utéza, O.; Delaporte, P. Multi-wavelength enhancement of silicon Raman scattering by nanoscale laser surface ablation. *Appl. Surf. Sci.* **2013**, *284*, 545–548. [CrossRef]
49. Russell, J.P. Raman scattering in silicon. *Appl. Phys. Lett.* **1965**, *6*, 223–224. [CrossRef]
50. Parker, J.H.; Feldman, D.W.; Ashkin, M. Raman Scattering by Silicon and Germanium. *Phys. Rev.* **1967**, *155*, 712–714. [CrossRef]
51. Uchinokura, K.; Sekine, T.; Matsuura, E. Raman scattering by silicon. *Solid State Commun.* **1972**, *11*, 47–49. [CrossRef]
52. Weinstein, B.A.; Piermarini, G.J. Raman scattering and phonon dispersion in Si and GaP at very high pressure. *Phys. Rev. B* **1975**, *12*, 1172–1186. [CrossRef]
53. Poborchii, V.; Tada, T.; Kanayama, T. Study of stress in a shallow-trench-isolated Si structure using polarized confocal near-UV Raman microscopy of its cross section. *Appl. Phys. Lett.* **2007**, *91*, 241902. [CrossRef]
54. Zhang, C.; Duan, Z. A model for C–O–H fluid in the Earth's mantle. *Geochim. et Cosmochim. Acta* **2009**, *73*, 2089–2102. [CrossRef]
55. Li, Z.; Bradt, R.C. Thermal Expansion of the Hexagonal (6H) Polytype of Silicon Carbide. *J. Am. Ceram. Soc.* **1986**, *69*, 863–866. [CrossRef]
56. Watanabe, H.; Yamada, N.; Okaji, M. Linear Thermal Expansion Coefficient of Silicon from 293 to 1000 K. *Int. J. Thermophys.* **2004**, *25*, 221–236. [CrossRef]
57. Arsenault, R.J.; Shi, N. Dislocation generation due to differences between the coefficients of thermal expansion. *Mater. Sci. Eng.* **1986**, *81*, 175–187. [CrossRef]

58. Vogelsang, M.; Arsenault, R.J.; Fisher, R.M. An *in situ* HVEM study of dislocation generation at Al/SiC interfaces in metal matrix composites. *MTA* **1986**, *17*, 379–389. [CrossRef]
59. Anastassakis, E.; Pinczuk, A.; Burstein, E.; Pollak, F.H.; Cardona, M. Effect of static uniaxial stress on the Raman spectrum of silicon. *Solid State Commun.* **1970**, *8*, 133–138. [CrossRef]
60. Hart, T.R.; Aggarwal, R.L.; Lax, B. Temperature Dependence of Raman Scattering in Silicon. *Phys. Rev. B* **1970**, *1*, 638–642. [CrossRef]
61. Cerdeira, F.; Buchenauer, C.J.; Pollak, F.H.; Cardona, M. Stress-Induced Shifts of First-Order Raman Frequencies of Diamond- and Zinc-Blende-Type Semiconductors. *Phys. Rev. B* **1972**, *5*, 580–593. [CrossRef]
62. Campbell, I.H.; Fauchet, P.M. The effects of microcrystal size and shape on the one phonon Raman spectra of crystalline semiconductors. *Solid State Commun.* **1986**, *58*, 739–741. [CrossRef]
63. Kouteva-Arguirova, S.; Arguirov, T.; Wolfframm, D.; Reif, J. Influence of local heating on micro-Raman spectroscopy of silicon. *J. Appl. Phys.* **2003**, *94*, 4946–4949. [CrossRef]
64. Georgi, C.; Hecker, M.; Zschech, E. Effects of laser-induced heating on Raman stress measurements of silicon and silicon-germanium structures. *J. Appl. Phys.* **2007**, *101*, 123104. [CrossRef]
65. Yang, Y.; Munck, K.D.; Teixeira, R.C.; Swinnen, B.; Verlinden, B.; Wolf, I.D. Process induced sub-surface damage in mechanically ground silicon wafers. *Semicond. Sci. Technol.* **2008**, *23*, 075038. [CrossRef]
66. Zhang, Y.; Wang, D.; Gao, W.; Kang, R. Residual stress analysis on silicon wafer surface layers induced by ultra-precision grinding. *Rare Met.* **2011**, *30*, 278–281. [CrossRef]
67. Xu, Z.; He, Z.; Song, Y.; Fu, X.; Rommel, M.; Luo, X.; Hartmaier, A.; Zhang, J.; Fang, F. Topic Review: Application of Raman Spectroscopy Characterization in Micro/Nano-Machining. *Micromachines* **2018**, *9*, 361. [CrossRef] [PubMed]
68. Robinson, P.T.; Bai, W.-J.; Malpas, J.; Yang, J.-S.; Zhou, M.-F.; Fang, Q.-S.; Hu, X.-F.; Cameron, S.; Staudigel, H. Ultra-high pressure minerals in the Luobusa Ophiolite, Tibet, and their tectonic implications. *Geol. Soc. Lond. Spec. Publ.* **2004**, *226*, 247–271. [CrossRef]
69. Zarudi, I.; Zhang, L. Subsurface damage in single-crystal silicon due to grinding and polishing. *J. Mater Sci. Lett.* **1996**, *15*, 586–587. [CrossRef]
70. Amelinckx, S.; Strumane, G.; Webb, W.W. Dislocations in Silicon Carbide. *J. Appl. Phys.* **1960**, *31*, 1359–1370. [CrossRef]
71. Dobrzhinetskaya, L.F.; Green, H.W.; Bozhilov, K.N.; Mitchell, T.E.; Dickerson, R.M. Crystallization environment of Kazakhstan microdiamond: evidence from nanometric inclusions and mineral associations. *J. Metamorph. Geol.* **2003**, *21*, 425–437. [CrossRef]
72. Kvasnytsya, V.M.; Wirth, R. Nanoinclusions in microdiamonds from Neogenic sands of the Ukraine (Samotkan' placer): A TEM study. *Lithos* **2009**, *113*, 454–464. [CrossRef]